Large Eddy Simulations of Isolated and Installed Jet Noise using the High-Order Discontinuous Galerkin Method

Daniel Lindblad*, Spencer J. Sherwin[†] and Chris D. Cantwell [‡]
Imperial College London, London, SW7 2AZ, United Kingdom

Jack L.T. Lawrence[§]
University of Southampton, Southampton, SO17 1BJ, United Kingdom

Anderson R. Proença[¶]
Cranfield University, Cranfield, MK43 0AL, United Kingdom

Margarida Moragues Ginard[‖]
Basque Center for Applied Mathematics, Bilbao, 48009, Spain

A recently developed computational framework for jet noise is used to compute the noise generated by an isolated and installed jet. The framework consists of two parts. In the first part, the spectral/hp element framework Nektar++ (www.nektar.info) is used to compute the near-field flow. Nektar++ solves the unfiltered Navier-Stokes equations on unstructured grids using the high-order discontinuous Galerkin method. The discrete equations are integrated in time using an implicit scheme based on the matrix-free Newton-GMRES method. In the second part, the Antares library (www.cerfacs.fr/antares/) is used to compute the far-field noise. Antares solves the Ffowcs Williams - Hawkings equation for a permeable integration surface in the time domain using a source-time dominant algorithm. The simulations are validated against experimental data obtained in the Doak Laboratory Flight Jet Rig, located at the University of Southampton. For the isolated jet, good agreement is achieved, both in terms of the flow statistics and the far-field noise. The discrepancies observed for the isolated jet are believed to be caused by an under-resolved boundary layer in the simulations. For the installed jet, the flow statistics are also well predicted. In the far-field, very good agreement is achieved for downstream observers. For upstream observers, some discrepancies are observed for very high and very low frequencies.

I. Nomenclature

Roman/Greek

c	=	speed of sound, m s^{-1}
D_j	=	diameter of nozzle, m
f	=	frequency, s^{-1}
M_a	=	acoustic Mach number
p	=	pressure, kg m^{-1} s^{-2}
P	=	polynomial degree
r	=	distance between microphone and nozzle exit, m
t	=	time, s
T	=	temperature, K
u_i	=	Cartesian velocity component, m s^{-1}

*Research Associate, Department of Aeronautics, South Kensington Campus, London SW7 2AZ.

[†]Professor, Department of Aeronautics, South Kensington Campus, London SW7 2AZ.

[‡]Senior Lecturer, Department of Aeronautics, South Kensington Campus, London SW7 2AZ.

[§]Senior Research Fellow, Institute of Sound and Vibration Research, Highfield, Southampton SO17 1BJ, Member AIAA.

[¶]Lecturer in Aerodynamics, School of Aerospace, Transport and Manufacturing, Cranfield, MK43 0AL, Member AIAA.

[‖]Marie Skłodowska-Curie Action-IF Researcher, Computational Mathematics, Alameda de Mazarredo 14, 48009 Bilbao.

U_j =   velocity at nozzle exit, m s^{-1}
ΔV =   volume of grid element, m^3
x_i =   Cartesian coordinate, m
γ =   ratio of specific heats
θ =   observer angle
μ =   dynamic viscosity, kg m^{-1} s^{-1}
ρ =   density, kg m^{-3}
τ =   sampling interval, s

Subscripts/Superscripts

$\square_\infty$ =   far-field value
$\square^*$ =   non-dimensional quantity

II. Introduction

JET noise has been one of the dominant sources of aircraft noise at take-off for over half a century. Further reductions in jet noise are therefore needed in order to meet the ambitious noise reduction goals set forward by the EU [1], and thereby minimize the negative impacts of commercial aviation.

The acoustic power of an isolated jet is proportional to the eighth power of the jet velocity [2, 3]. By lowering the jet velocity, the noise produced by an isolated jet can therefore be reduced substantially. In order to accomplish this, while at the same time maintaining the required thrust levels, high bypass ratio turbofan engines have been introduced. However, as the bypass ratio of the engine increases, so does its diameter. This, in turn, requires the engines to be installed closer to the wings in order to maintain sufficient ground clearance.

It has been known for long that the presence of a solid boundary, such as a wing, can greatly influence the noise sources present in, e.g., a turbulent jet [4, 5]. The first evidence that this also applies to jet noise was provided by Bushell [6], who compared the noise produced by isolated jets under static conditions with the noise generated by installed jets under flight conditions. Since then, a lot of research has focused on identifying and quantifying the noise sources of installed jets [7, 8]. It has been found that installed jets produce additional low frequency noise which has a dipole-like directivity. This additional noise is generated when near-field evanescent waves are scattered by the trailing edge of the wing [9]. For installed jets, it has also been shown that the high frequency noise decreases above the wing and increases below the wing as a result of shielding and reflection, respectively [7–9].

High fidelity simulations of turbulent jets are an important tool for understanding and quantifying jet noise. Unfortunately, Direct Numerical Simulations (DNS) of turbulent jets operating at realistic Reynolds numbers will remain prohibitively expensive within the foreseeable future [10]. Therefore, the Large Eddy Simulation (LES) technique, in which the largest turbulent scales are resolved, and the remaining scales are modeled, is commonly used to study jet noise [10–12]. Most studies of jet noise to date have used a finite volume or a finite difference method to discretize the governing equations in space, see e.g. [13–23] and [24–31]. In some of these studies, a subgrid-scale model is used to account for the unresolved turbulent scales [14, 16–19, 21–23, 31]. The remaining studies use a filter and/or the dissipation introduced by the spatial discretization for the same purpose [13, 15, 20, 24–30]. The grid topology also differs between different studies. In [16, 17, 20–23, 28, 31], different types of unstructured or hybrid structured-unstructured grids are used, whereas in [13–15, 18, 19, 24–27, 29, 30], structured grids are used. In general, unstructured grids are geometrically more versatile than structured grids. However, when a finite volume or a finite difference method is used, it is typically easier to formulate a high-order discretization on a structured grid.

In addition to the finite volume and the finite difference methods, other discretization schemes exist. These include, but are not limited to, the discontinuous Galerkin (DG) method [32, 33], the flux reconstruction (FR) method [34], the spectral-difference (SD) method [35–38], and the continuous Galerkin (CG) method [39]. Common to all these methods is that they can reach a high order of accuracy on unstructured grids. This makes them interesting for studying the noise generated by complex flows, such as turbulent installed jets.

However, apart from a few studies to date [40, 41], the use of the DG, FR, SD and CG methods for jet aeroacoustics appears to be limited. Therefore, the purpose of this work is to further explore the capabilities of the DG method in the context of jet aeroacoustics. To this end, a recently developed computational framework [41] based on the open-source spectral/hp element framework Nektar++ [42–45] and the Antares library [46–48] is used to predict the noise generated by an isolated and installed jet. This jet was recently tested in the Doak Laboratory Flight Jet Rig (FJR), located at the

University of Southampton [49]. Experimental results obtained in the FJR will be used to validate the computational framework presented in this paper.

III. Case Description

The nozzle considered in this work has an inner diameter of $D_j = 40$mm, a convergence half-angle of $2.44°$, and a total length of $19D_j$. Both an isolated and an installed configuration are considered. In the installed configuration, an uniform-chord (2D) NACA4415 airfoil at $4°$ angle of attack is mounted near the nozzle. The axial and vertical distance between the nozzle exit and the airfoil trailing edge are $L = 3D_j$ and $H = 0.6D_j$, respectively. The chord and span of the airfoil are $3.75D_j$ and $15D_j$, respectively. A schematic view of the installed configuration is shown in Fig. 1.
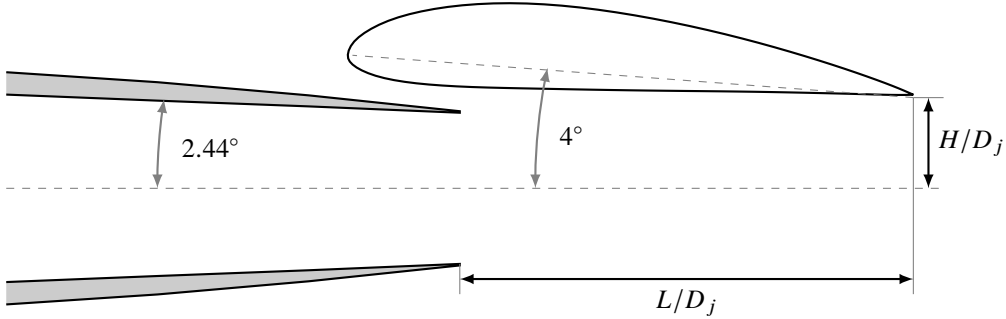
Fig. 1   Schematic view of the nozzle installed under the wing.

In this work, we consider a single operating point of the nozzle, corresponding to an acoustic Mach number of $M_a = U_j/c_\infty = 0.6$, a Reynolds number of $Re_j = \rho_\infty U_j D_j/\mu_\infty = 5.5 \cdot 10^5$, and a static temperature ratio of $T_j/T_\infty = 0.9335$. No co-flow (flight stream) is considered.

IV. Numerical Method

This section gives a brief overview the numerical method used to compute the far-field noise. The computation is split into two parts. In the first part, the turbulent jet is simulated using Nektar++. The solution obtained with Nektar++ is then exported to Antares, which uses the Ffowcs Williams - Hawkings method to compute the far-field noise. More details on the computational framework can be found in [41].

A. Flow Solver

The near-field flow is computed using the compressible flow solver implemented in the spectral/hp element framework Nektar++ [42–45]. The compressible flow solver in Nektar++ solves the Navier-Stokes equations in coupled, conservative form using the high-order discontinuous Galerkin (DG) method. In the DG method, the solution in each mesh element is expressed as a high-order polynomial of degree P. As the name of the method suggest, the solution is not continuous at element interfaces. Instead, the solutions in adjacent elements are coupled by computing a numerical flux across element boundaries. In this work, we use Roe's approximate Riemann solver [50] and the Interior Penalty (IP) method [51] to compute the convective and diffusive fluxes, respectively. Details on how the Riemann solver is implemented can be found in [52]. The implementation of the IP method is further described in [45].

Unresolved turbulent scales are accounted for using an implicit Large Eddy Simulation (iLES) approach. In this approach, the numerical dissipation introduced by the discretization is used instead of a subgrid-scale model to dissipate the smallest resolved scales. Previous work has shown that the DG method in combination with Roe's approximate Riemann solver is well suited for this purpose [53–59].

The discrete set of equations obtained from the spatial discretization are integrated in time using a second-order, singly diagonally implicit Runge-Kutta method. The nonlinear system obtained from the temporal discretization is solved using a preconditioned, matrix-free Newton-GMRES algorithm [60], see [45] for details.

Following [16], we non-dimensionalize the Navier-Stokes equations using the diameter of the nozzle, the density in the far-field, the speed of sound in the far-field, and the temperature in the far-field. This leads to the following non-dimensional quantities

$$\rho^* = \frac{\rho}{\rho_\infty}, \quad u_i^* = \frac{u_i}{c_\infty}, \quad p^* = \frac{p}{\rho_\infty c_\infty^2} = \frac{p}{\gamma p_\infty}, \quad T^* = \frac{T}{T_\infty}, \quad t^* = \frac{t c_\infty}{D_j}, \quad x_i^* = \frac{x_i}{D_j}. \tag{1}$$

Here, $\square^*$ denotes a non-dimensional quantity, $\square_\infty$ denotes a far-field value, $\gamma = 1.4$ is the ratio of specific heats, and D_j is the diameter of the nozzle. In this work, we assume that the gas is calorically perfect and obeys the ideal gas law. Since the nozzle is close to isothermal, we also assume that the viscosity is constant and equal to the far-field value. Under these assumptions, the non-dimensional viscosity and thermal conductivity can be computed as

$$\mu^* = \frac{M_a}{Re_j}, \quad k^* = \frac{\mu^*}{(\gamma - 1)Pr}. \tag{2}$$

Here, $M_a = U_j/c_\infty$ is the acoustic Mach number, $Re_j = \rho_\infty U_j D_j/\mu_\infty$ is the Reynolds number, and $Pr = 0.72$ is the Prandtl number. The ideal gas law expressed in terms of non-dimensional quantities finally reads

$$p^* = \frac{\rho^* T^*}{\gamma}. \tag{3}$$

B. Far-Field Noise Prediction

The far-field noise is computed using the Antares library [46–48]. Antares solves the Ffowcs Williams - Hawkings equation [61] for a permeable integration surface [62] in the time domain using a source-time dominant algorithm. At present, Antares provides two solution formulations, Formulation 1A by Farassat [63] and Formulation 1C by Najafi-Yazidi et al. [64]. The main difference between these two formulations is that the latter includes the effects of a flight stream on noise propagation. Since no flight stream is considered in this work, Formulation 1A is used.

Like most LES studies of jet noise to date, we don't include the volume integral in the solution to the Ffowcs Williams - Hawkings equation. This simplification is valid as long as the integration surface encloses all relevant noise sources [62], and no significant entropy or vorticity waves cross the integration surface [13, 65]. In LES computations of turbulent jets, the latter condition is typically hard to satisfy at the downstream end of the integration surface [13, 65, 66]. As a result, spurious noise is generated when entropy and/or vorticity waves cross the integration surface. To solve this problem, the method of end-caps [13] is often used, see e.g. [16, 17, 21]. Alternatively, the integration surface can be left open at the downstream end [19, 22, 31, 40, 67]. In this work, we use the latter option.

Antares is used to compute the non-dimensional pressure signal at the same microphone locations as in the experiments, see Fig. 2. After this, the power spectral density (PSD) is computed from the non-dimensional pressure signal using the implementation of Welch's method [68] available in SciPy v1.2.1 [69]. In this work, we use a 50% overlap and a Hann window function for Welch's method. For the isolated jet, we also average the PSD over 36 microphones placed uniformly around the circumference. This helps to compensate for the relatively short time signal that is obtained from the simulations. More details on how the PSD is computed can be found in [41].

The PSD obtained from the above procedure is non-dimensional. In order to compare with experiments, we scale the PSD using the ambient conditions measured in the experiments. More precisely, we compute the PSD in $[\text{dB}/St]$ as

$$\text{PSD}(St) = 10 \log_{10} \left(\frac{(\gamma p_\infty)^2 M_a \hat{P}^*(St M_a)}{p_{\text{ref}}^2} \right) + 20 \log_{10} \left(\frac{r}{r_{\text{ref}}} \right). \tag{4}$$

Here, $St = f D_j/U_j$ is the Strouhal number, $M_a = U_j/c_\infty$ is the acoustic Mach number, $\hat{P}^*(f^*)$ is the non-dimensional PSD, and $p_{\text{ref}} = 20 \cdot 10^{-6}$ Pa is the reference pressure. To stay consistent with the post-processing procedure used for the experimental data, we also scale the PSD to $r_{\text{ref}} = 1$m distance by adding $20 \log_{10}(r/r_{\text{ref}})$, where r is the distance between the microphone and the nozzle exit (in meters).
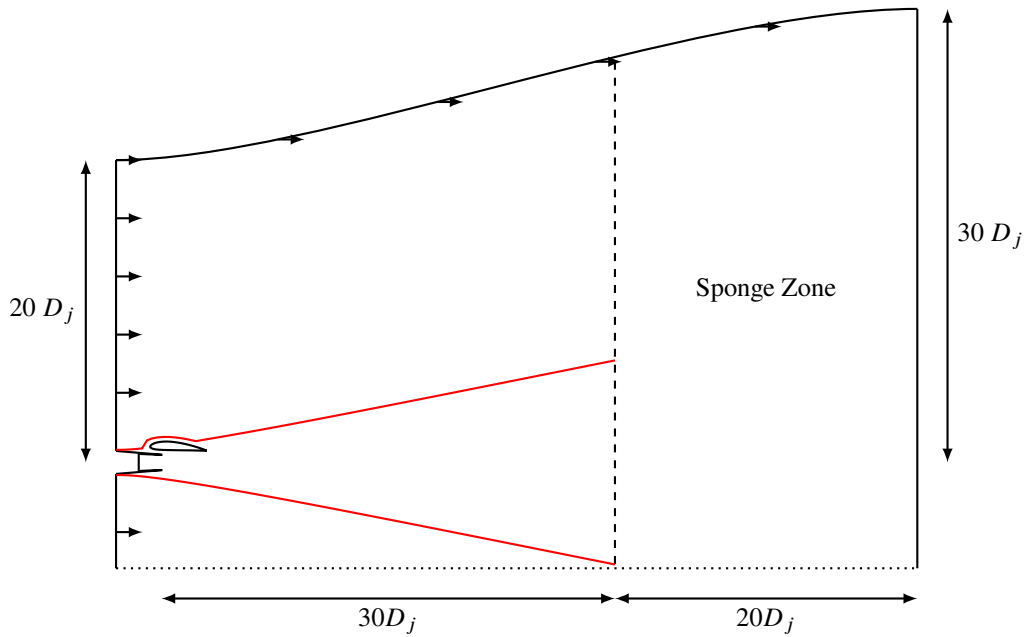
C. Computational Setup

1. Computational Domain and Boundary Conditions

An axisymmetric, funnel-shaped, computational domain is used for all simulations considered in this work. A schematic view of the computational domain is presented in Fig. 3. As can be seen from this figure, the domain extends $30D_j$ radially and $50D_j$ axially away from the nozzle exit.
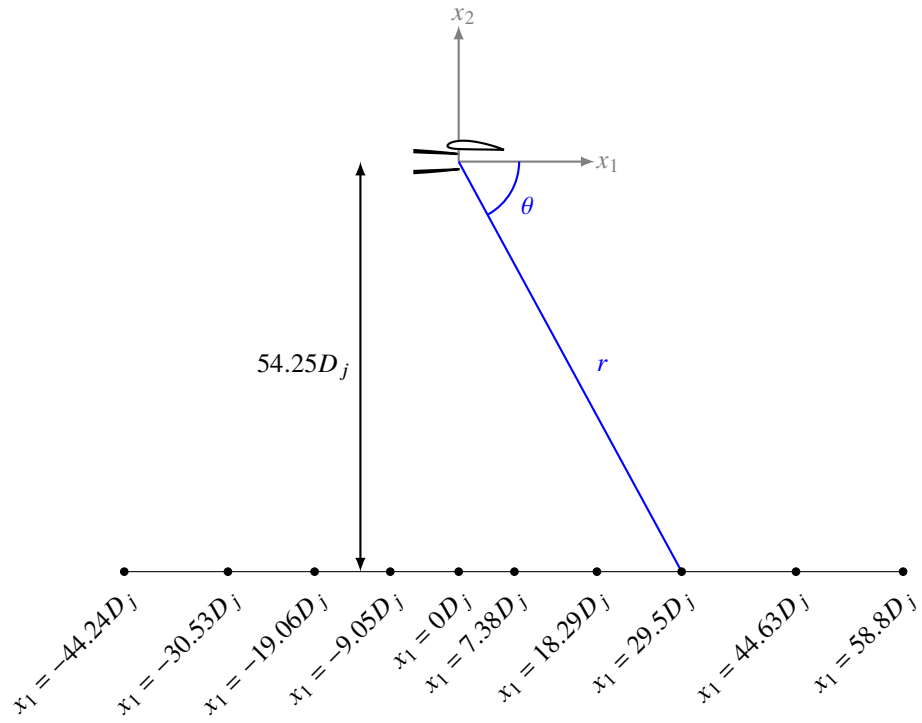
Fig. 2   Schematic view showing the locations of the far-field microphones and the definition of the observer angle.

Fig. 3   Schematic view of the computational domain and the Ffowcs Williams - Hawkings integration surface.

The inlet to the nozzle is placed $1.5D_j$ upstream of the nozzle exit. At this boundary, non-uniform profiles of stagnation temperature and pressure are imposed. These profiles are selected to ensure that the mean velocity matches the experimental data as closely as possible at the nozzle exit. In addition to the mean velocity, several studies have demonstrated the importance of getting the turbulence levels at the nozzle exit right [21, 27]. To satisfy this condition, the boundary layer must be sufficiently well resolved. In addition to this, some technique for tripping the boundary layer into a turbulent state may be needed [21, 67, 70], especially if only a short part of the nozzle is included in the simulation. In this work, no attempt at tripping the boundary layer has been made. As will be explained in more detail later, the resolution close to the nozzle wall is also relatively low. This typically motivates the use of a wall-model. Unfortunately, Nektar++ currently does not provide any wall models. Therefore, a no-slip boundary condition is used for all walls instead. The wall modeling used in this work may therefore lead to some discrepancies in terms of turbulence levels at the nozzle exit.

Along the far-field boundaries, we add a small co-flow corresponding to 2% of the jet velocity. This is done to ensure that vortical structures generated in the jet are removed from the domain, and to facilitate flow entrainment. All boundary conditions are imposed weakly through the Riemann solver [52]. This implies that the far-field boundaries, where a complete thermodynamic state is imposed, will be non-reflecting for normally incident waves if the Riemann solver correctly differentiates between incoming and outgoing waves. The Riemann solver selected in this work approximately satisfies this condition.

Finally, at the outlet, the far-field static pressure is imposed. This boundary condition is perfectly reflective. Therefore, we add a sponge zone [71] upstream of the outlet, see Fig. 3. In this zone, the right-hand side of the governing equations is augmented with a damping term in order to drive the solution towards a steady reference state. In this work, the reference state is obtained with STAR-CCM+ v2019.2 using the $k - \omega$ SST turbulence model. More details on how the sponge zone is implemented is presented in [41].

2. Computational Mesh

An unstructured mesh topology has been developed for the nozzle configurations considered in this work. To generate the mesh, the CAD is first imported into the open-source mesh generator Gmsh [72]. In Gmsh, the OpenCASCADE CAD kernel is used to clean up the CAD and add the missing boundaries. To facilitate this step, we make extensive use of constructive solid geometry. For example, to include the wing in the simulation, we subtract the wing from the computational domain used for the isolated jet. After the domain boundaries have been constructed, Gmsh is also used to generate a triangular surface mesh. The surface mesh is then imported into STAR-CCM+ v2019.2, which is used to generate the volume mesh. In particular, the *Advancing Layer Mesher* and the *Tetrahedral Mesher* in STAR-CCM+ are used to create a single prism layer around all walls, and the remaining volume mesh, respectively. In the final step of the meshing process, the NekMesh utility [43], which is a part of the Nektar++ framework, is used to generate a high order mesh with several prism layers along the the nozzle wall. To this end, the mesh is first projected onto the underlying CAD by "curving" the triangular faces on the wall such that they conform to the CAD surface. After this, the mesh is checked for self-intersecting, and thereby invalid, elements. Such elements may be created when high aspect ratio prism elements are projected onto a highly curved surface. If invalid elements exist, they are linearized by removing the curvature, thereby restoring them to their original shape. For a high-quality volume mesh, this is typically only necessary for a handful of elements, and will thus not affect the simulation results significantly. Finally, in the last step, the curved prism elements are split in the wall-normal direction using an isoparametric approach [73]. The benefit of this approach is that it can generate valid, high aspect ratio, prism elements around curved geometries. More details on how the high-order mesh generation is set up in NekMesh can be found in [43].

The aforementioned procedure was used to generate three meshes, two for the isolated jet and one for the installed jet. These meshes are illustrated in Fig. 4. The first mesh, denoted "Mesh-1", is shown in Fig. 4a and 4b. This mesh was used in [41] to study the noise generated by the isolated jet. Based on lessons learned from this study, the second mesh, denoted "Mesh-2", was developed, see Fig. 4c and 4d. The second mesh is designed to better resolve the first $10D_j$ of the shear layer, i.e., the region before the end of the potential core. The refinement zones have also been adjusted to better reflect the position of the integration surface used for the far-field noise prediction. The third mesh, denoted "Mesh-3", is almost identical to "Mesh-2", except that it is slightly coarser further downstream and includes the wing. The third mesh is illustrated in Fig. 4e and 4f.

In all three meshes, the boundary layer is discretized with 13 elements in the wall normal direction, and one element per boundary layer thickness in the streamwise and spanwise directions. Although each element contains more than one degree of freedom in the DG method, this resolution is only sufficient for resolving the mean velocity profile. For
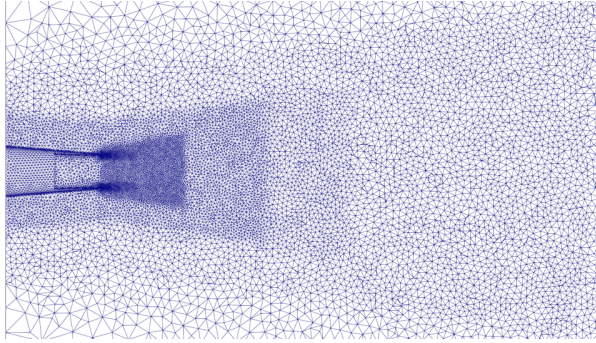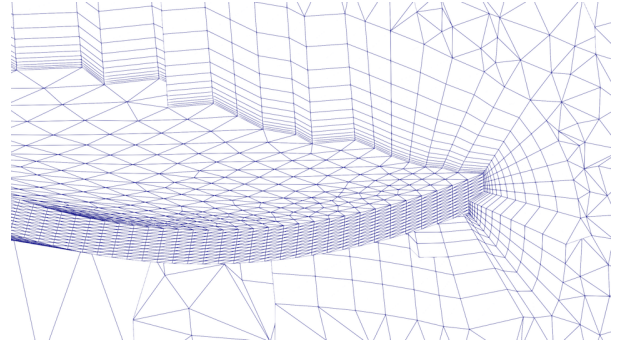
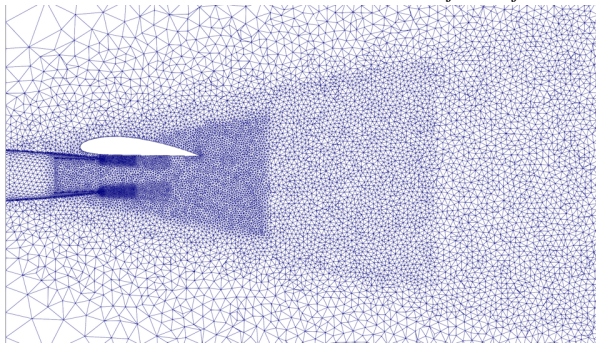(a) Overview of Mesh-1 for $x_1 \in (-3D_j, 15D_j)$.
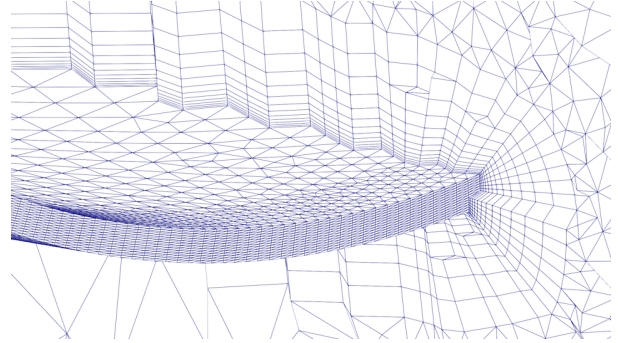
(b) Prism layer mesh for Mesh-1.
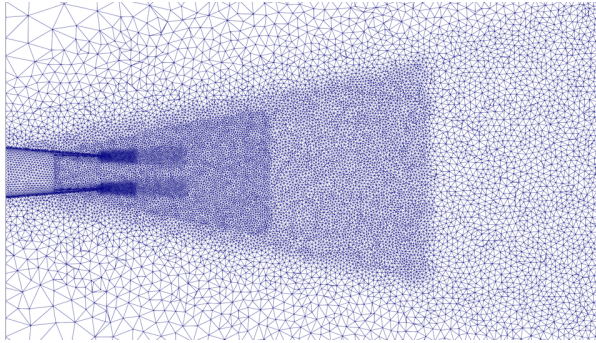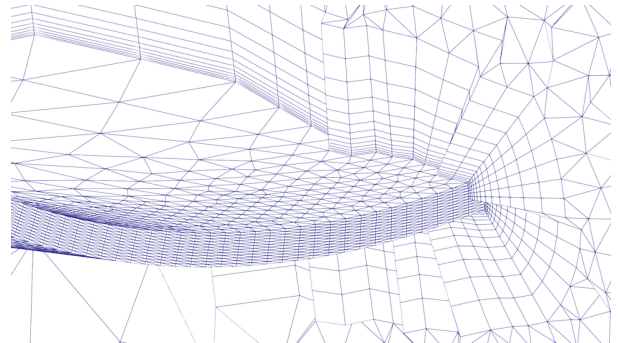

(c) Overview of Mesh-2 for $x_1 \in (-3D_j, 15D_j)$.

(d) Prism layer mesh for Mesh-2.

(e) Overview of Mesh-3 for $x_1 \in (-3D_j, 15D_j)$.

(f) Prism layer mesh for Mesh-3.

Fig. 4   Illustration of unstructured grids defined in Table 1.

wall-modeled or wall-resolved LES, the resolution in the streamwise and spanwise direction would need to be higher [74].

As shown in Figs. 4b, 4d, and 4f, we use anisotropic mesh elements on the nozzle lip. This is done to ensure that the last layer of prism elements is isotropic. The size of the surface elements is further chosen such that the size of the triangular faces at the top of the prism layer matches the size of the tetrahedral elements. A summary of all meshes used in this work is provided in Table 1.

Table 1 Mesh settings.

Name	Configuration	N_{prism}	N_{tet}
Mesh-1	Isolated	$5.94 \cdot 10^5$	$4.14 \cdot 10^6$
Mesh-2	Isolated	$4.36 \cdot 10^5$	$6.18 \cdot 10^6$
Mesh-3	Installed	$4.63 \cdot 10^5$	$4.54 \cdot 10^6$

3. Simulation Parameters

A total of 4 simulations have been performed in this work, 2 for the isolated jet and 2 for the installed jet. The simulations of the isolated jet were performed with a polynomial degree of $P = 2$. In the first simulation, Mesh-1 was used, and in the second simulation, Mesh-2 was used. The remaining two simulations of the installed jet were performed on Mesh-3. In the first simulation, a polynomial degree of $P = 2$ was used, and in the second one, $P = 3$ was used.

The two simulations of the isolated jet were initialized with a steady RANS solution obtained with STAR-CCM+ v2019.2 using the $k - \omega$ SST turbulence model. After this, each simulation was run for 350 non-dimensional (acoustic) time units to bypass the initial transient. Finally, the simulations were run for another 320 non-dimensional time units. During this time, the conservative variables were sampled every 20th time step at a set of linear arrays in the jet plume. Since the flow is statistically axisymmetric for the isolated jet, 8 arrays were placed uniformly around the circumference such that statistical quantities could be averaged. In addition to the near-field sampling, the flow was also sampled at the integration surface used for the Ffowcs Williams - Hawkings method. In this work, we use a conical surface that has a radius of $0.75D_j$ at the nozzle exit, and a spreading rate of 0.2. Earlier work has shown that this surface is wide enough to enclose all relevant noise sources [41]. In the first simulation, the flow was sampled every 40th time step at the integration surface, whereas for the second simulation, the flow was sampled every 20th time step. The higher frequency was used to match the higher resolution of Mesh-2. The time step used in the simulations of the isolated jet was set to $\Delta t^* = 0.002$.

The first simulation of the installed jet was initialized from a steady RANS solution obtained with STAR-CCM+. Since the installed jet does not possess the same symmetry as the isolated one, it was run for 450 non-dimensional time units before the sampling was started. The second simulation of the installed jet, which was run at $P = 3$, was started from the $P = 2$ solution at $t^* = 250$. After this, it was run for another 300 non-dimensional time units before sampling began. The first simulation was sampled for 900 non-dimensional time units, whereas the second one was only sampled for 300 non-dimensional time units, due to the higher computational cost associated with the higher polynomial degree. During sampling, the conservative variables were saved every 20th time step at a set of linear arrays in the jet plume. However, since the installed jet is not axisymmetric, additional arrays for averaging statistical quantities in the circumferential direction were not used. The flow was also stored every 20th time step at the Ffowcs Williams - Hawkings integration surface. This surface was constructed by combining the conical surface used for the isolated jet with a wing-shaped surface that encloses the wing. This relatively simple topology is believed to be sufficient since no flight stream is considered, which in turn means that the wing does not create a wake and/or wing-tip vortex. If the effect of a flight stream is considered, more sophisticated surfaces should be used [22]. The time step used for the installed jet was also set to $\Delta t^* = 0.002$.

In [17], the highest resolved Strouhal number is estimated from the LES resolution at the integration surface and the number of points per wavelength required by the spatial discretization. Since the dissipation and dispersion properties of the DG method depend on both the mesh size and the polynomial order [57], we use a generalized equation for computing the highest resolved Strouhal number, originally proposed in [41]

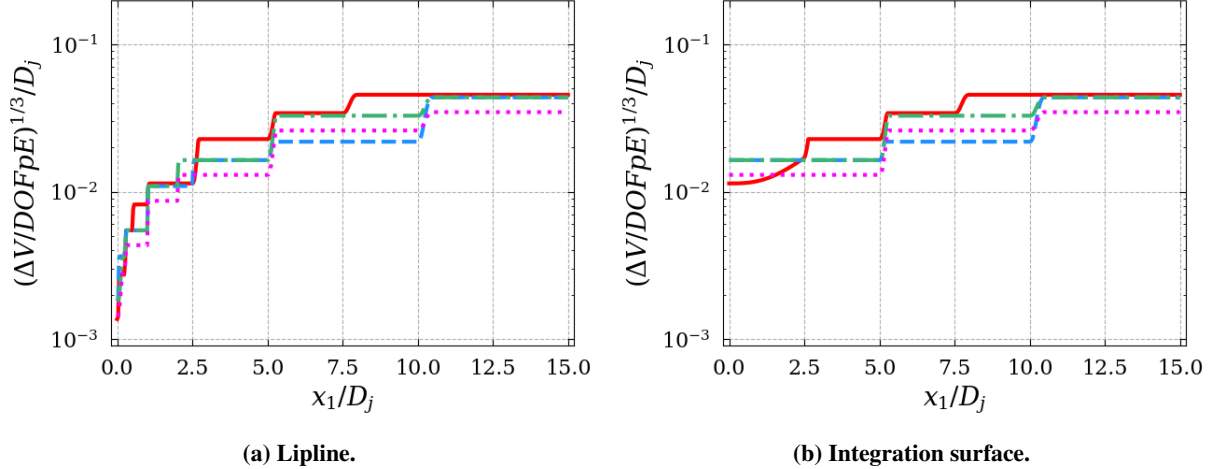$$St_{\text{lim}} = \frac{D_j (DOFpE/\Delta V)^{1/3}}{M_a \, DOFpW}. \tag{5}$$

(a) Lipline.   (b) Integration surface.

Fig. 5   Equivalent mesh size: Isolated-1 (——), Isolated-2 (- - - -), Installed-1 (-·-·-), Installed-2 (·······).

Here, $DOFpE$ denotes the number of basis functions that span the polynomial space inside each element, ΔV denotes the volume of a grid element at the integration surface, and $DOFpW$ denotes the number of degrees of freedom per wavelength required by the spatial discretization.

To compute the highest resolved Strouhal number based on Eq. (5), we start by computing $(\Delta V/DOFpE)^{1/3}/D_j$ along the integration surface. Note that this property can be interpreted as an "equivalent mesh size" for the high-order DG discretization. The results for all combinations of mesh sizes and polynomial degrees used in this work are shown in Fig. 5b. As can be seen from this figure, the equivalent mesh size is not constant along the integration surface, owing to the expanding grid size. As explained in [21], the high-frequency noise sources are located between the nozzle exit and the end of the potential core, i.e, in the region $0 < x_1/D_j < 10$. Therefore, we chose the largest value of the equivalent mesh size within this range to estimate St_{lim}. The value of $DOFpW$ is then obtained using the 1% rule suggested by Moura et al. [57]. Combined with the acoustic Mach number of the jet, these values give the estimates of St_{lim} shown in Table 2. In this table, a summary of the settings used for each simulation is also provided.

Table 2   Simulation settings. Δt_{jet} and Δt_{FW-H} denote the sampling interval in the jet plume and on the Ffowcs Williams - Hawkings integration surface, respectively. τ_{init} and τ_{sample} denote the time the simulation is run before sampling and during sampling, respectively.

| Name	P	Mesh	DOF	Initialize from	$\frac{\Delta t c_\infty}{D_j}$	$\frac{\Delta t_{jet} c_\infty}{D_j}$	$\frac{\Delta t_{FW-H} c_\infty}{D_j}$	$\frac{\tau_{init} c_\infty}{D_j}$	$\frac{\tau_{sample} c_\infty}{D_j}$	St_{lim}
Isolated-1	2	Mesh-1	$52 \cdot 10^6$	RANS	0.002	0.04	0.08	350	320	5.1
Isolated-2	2	Mesh-2	$70 \cdot 10^6$	RANS	0.002	0.04	0.04	350	320	10.5
Installed-1	2	Mesh-3	$54 \cdot 10^6$	RANS	0.002	0.04	0.04	450	900	7.0
Installed-2	3	Mesh-3	$109 \cdot 10^6$	Installed-1	0.002	0.04	0.04	300	300	11.1

V. Experimental Setup

The experimental data used in this paper were recorded in the Doak Laboratory Flight Jet Rig (FJR), located at the University of Southampton. The following sub-sections present information about the facility, instrumentation, and experimental data post-processing.

A. Facility and Hardware

The Doak Laboratory is an anechoic chamber, fully anechoic above 400 Hz with dimensions approximately equal to 15 m-long, 7 m-wide and 5 m-high. The recently commissioned Flight Jet Rig (FJR) consists of two separate air supply systems that allow in-flight simulations of single-stream, subsonic jet flows. The primary 'core' jet flow is supplied by a

high-pressure compressor-reservoir system, capable of producing a maximum inlet pressure of 20 Bar. The secondary 'flight' jet flow is supplied by a 1.1 pressure ratio fan. The 300 mm-diameter flight nozzle can produce flow velocities up to Mach 0.3. Photographs of the Doak Laboratory during the far-field, near-field, and flow-field campaigns are displayed in Fig. 6. Further information about the Doak Laboratory, the FJR, and the flight and core jet nozzles can be found in reference [49].
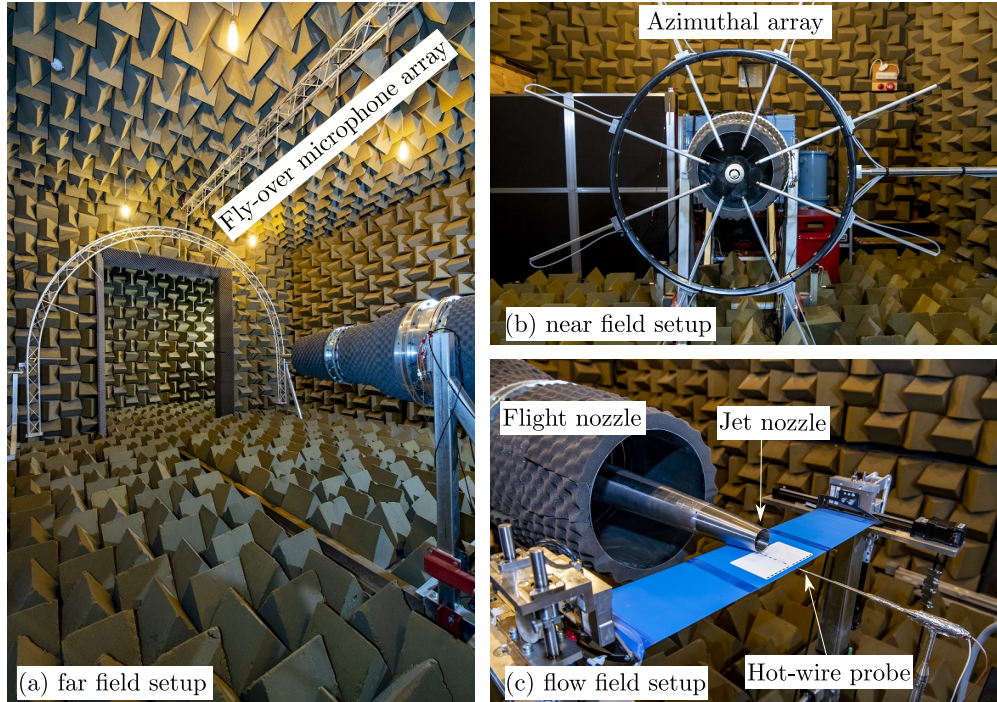
Fig. 6   Photographs of the Flight Jet Rig (FJR) in the Doak Laboratory at the University of Southampton.

B. Instrumentation

A DANTEC StreamLine Pro constant temperature anemometry system was used to acquire the instantaneous velocity field and local flow temperature data. A DANTEC 55P11 miniature platinum-plated tungsten hot-wire probe, held by a DANTEC 55H22 right-angled probe support, was attached to an ISEL 3-axis traverse system, which allowed 600 mm-stroke (i.e., $15D_j$) independent movement along each of the x, y and z planes. Less exhaustive tests using DANTEC 55P61 cross-wires were also performed. A DANTEC 90P10 total temperature probe was secured near the sensors to account for local temperature variations in the flow. The hot-wire and cross-wire probes were calibrated at both the start and end of the test campaign using a DANTEC StreamLine automatic calibrator over the velocity range 1 - 300 m/s. The calibration coefficients were then extracted using a fourth-order polynomial curve fit. Finally, a directional calibration was carried out for the cross-wire probes to obtain information on the transverse velocity component pf the flow field.

To obtain far-field pressure data, ten 1/4" B&K Type 4939 microphone capsules with B&K Type 2670 Falcon preamplifiers were fixed to the end of 0.5m-long aluminium tubes and secured to a linear aluminium truss on the ceiling of the laboratory (i.e., at $\phi = 0°$) such that each microphone diaphragm was parallel to the jet axis. The microphones were positioned to record data at observer polar angles between $\theta = 40°$ and $\theta = 130°$, at $10°$ intervals. Each microphone was calibrated at both the start and end of the test campaign using a 94dB 1000kHz tone generated by a SVANTEK SV30A calibrator.

The near-field azimuthal microphone array consisted of eight 1/4" B&K Type 4939 microphone capsules with B&K Type 2670 Falcon preamplifiers fixed at the end of 0.5m-long aluminium tubes. The tubes were threaded through machined holes in aluminium blocks secured to a rigid aluminium alloy ring at $\Delta\phi = 45°$ intervals and then held in place with nylon grub screws such that each microphone pointed directly at the centre of the ring. The ring was then attached to an ISEL 2-axis traverse system and aligned with the jet axis using a nozzle laser jig.

C. Data Acquisition and Data Post-Processing

Both the hot-wire and microphone unsteady voltage data were digitised using a National Instruments PXIe-4497 Dynamic Signal Analyser at a sample rate of 200 kHz with 24-bit resolution. The hot-wire signals were acquired for 5 seconds, corrected first for temperature, using the standard method as reported by DANTEC [75], and then for velocity using the 4th-order polynomial calibration coefficients. Both the near-field and far-field microphone signals were acquired for 10 seconds, filtered using a 20 Hz high-pass filter and then amplified using B&K Type 2690 Nexus amplifiers. The time signals were corrected for amplifier gain and microphone capsule calibration sensitivity before being transformed into the frequency domain using a Hamming window-averaged Fast Fourier Transform following Welch's overlapped segment-averaging spectral estimation method. The far-field spectra were then corrected for electronic background noise, atmospheric absorption, microphone incidence angle and distance (assuming spherical wave propagation) to yield the final free-field, 1m-lossless values. The static jet near-field spectra were only corrected for electronic background noise and microphone incidence.

Finally, the various steady rig flow control data were digitised using the data acquisition hardware described above. Mean values were extracted from the voltage time histories before the appropriate calibration transfer function constants were applied. The total temperatures of the flight and core jet flows were recorded directly using two National Instruments USB-TC01 devices.

VI. Results

A. Instantaneous Flow Field

The instantaneous flow fields obtained with all simulations considered in this work are illustrated by Mach number contours and contours of normalized pressure perturbations in Fig. 7. We start by considering Figs. 7a and 7b, which show the instantaneous flow field obtained with the Isolated-1 and the Isolated-2 simulation, respectively. As can be seen from these figures, the two simulations give very similar results. There are, however, some differences further downstream, where the higher resolution in the Isolated-2 simulation leads to a more detailed turbulent flow.

Next, we turn to Figs. 7c and 7d, which show the instantaneous flow field obtained with the Installed-1 and Installed-2 simulation, respectively. The first thing that can be noted from these figures is that there is a strong noise source located close to the trailing edge of the wing. This noise source is generated when evanescent pressure waves in the shear layer are scattered by the trailing edge. It is typically the dominant source at low Strouhal numbers, and radiates most efficiently in the flyover direction, i.e., at 90° to the jet axis. When comparing Figs. 7c and 7d, it is clear that the amplitude and wavelength of the acoustic waves that radiate away from the trailing edge are quite different. This is an indication that the pressure waves being scattered by the trailing edge are quite different in the two simulations, which in turn should be related to the state of the boundary layer and the early shear layer.
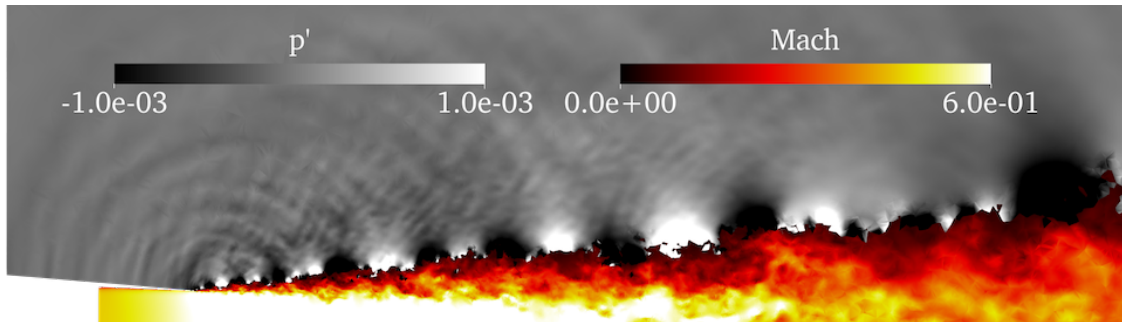
B. Flow Statistics

The mean axial velocity at the nozzle exit ($x_1/D_j = 0.005$) is shown in Fig. 8a. As can be seen from this figure, all simulations give virtually identical results. This is expected since the wing should not affect the flow inside the nozzle when there is no flight stream. The agreement between the simulations and the experimental data (obtained for the isolated jet) is also quite good. This is also expected since we impose tailored profiles of stagnation temperature and pressure at the nozzle inlet, see section IV.C for details.

Next, we turn to Fig. 8b, which shows the RMS of the axial velocity at the nozzle exit. As can be seen from this figure, the simulations that have been run with $P = 2$ underpredict the turbulence levels at the nozzle exit. As a result, the initial part of the shear layer will not be fully turbulent in these simulations, which in turn may lead to higher noise levels in the far-field [21, 27, 67]. The last simulation, denoted Installed-2 in Table 2, was run with $P = 3$. As can be seen from Fig. 8b, this leads to higher turbulence levels at the nozzle exit, which in turn may contribute to lower noise levels in the far-field, and thereby better agreement with the experimental data.

The mean and RMS of the axial velocity at several axial locations in the jet plume are shown in Fig. 9. We start by considering Fig. 9a, which shows the mean axial velocity for the isolated jet. As can be seen from this figure, the two simulations of the isolated jet agree quite well with the experimental data. The most notable discrepancy is found close to the centerline, where the simulations overpredict the mean velocity downstream of the potential core. If we turn to Fig. 9b, which shows the RMS of the axial velocity in the jet plume, we see that the agreement between the simulations and the experiments is once again very good, except close to the centerline, where the simulations underpredict the
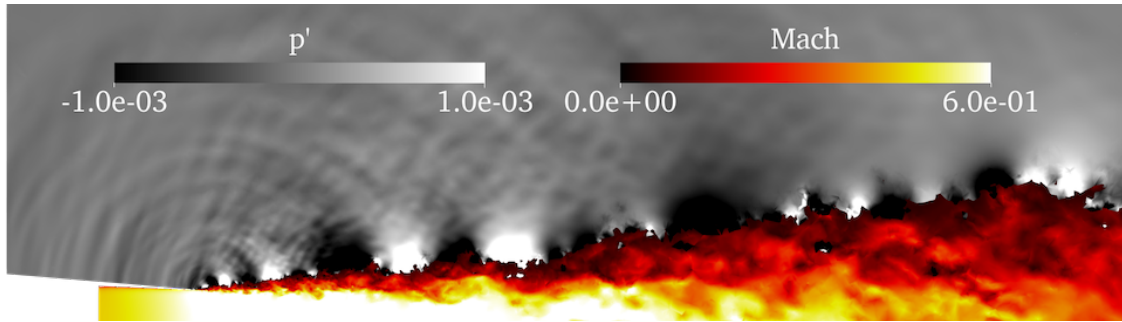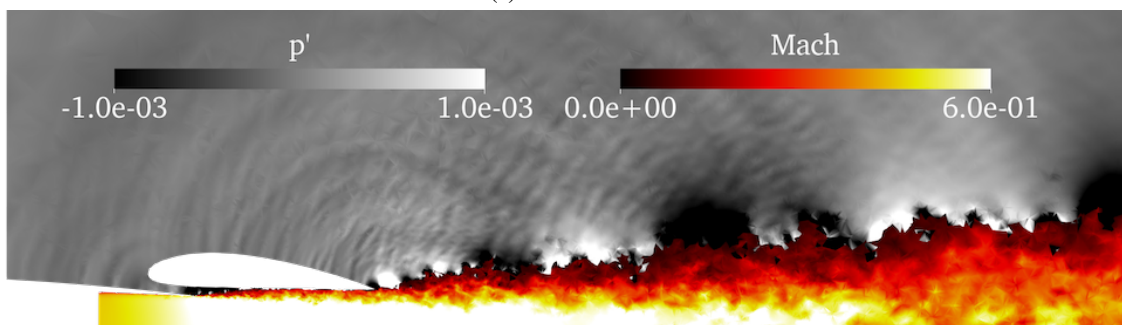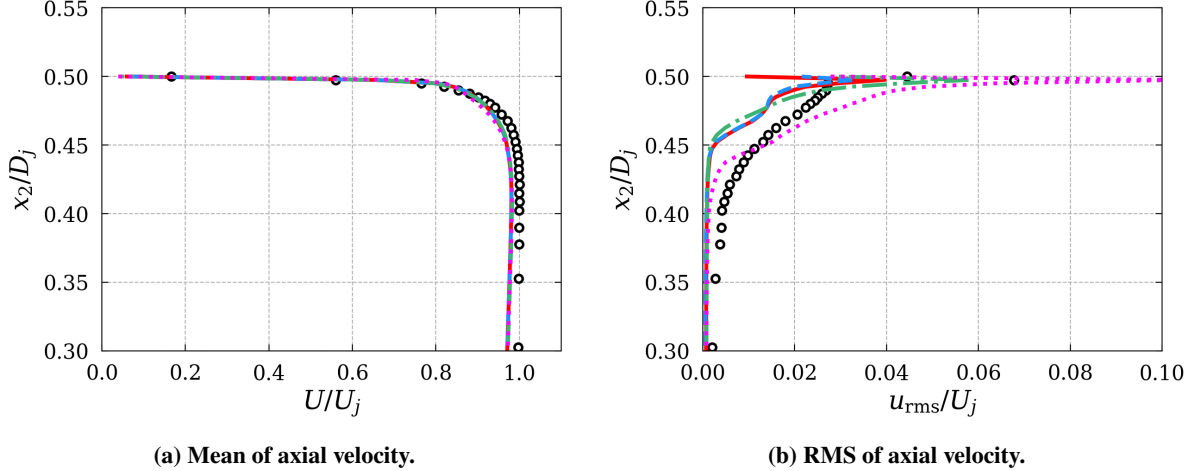
(a) Isolated-1.

(b) Isolated-2.
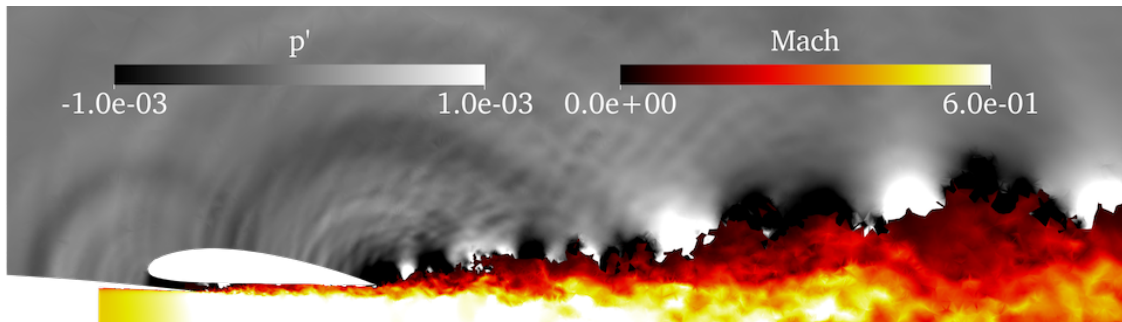
(c) Installed-1.

(d) Installed-2.

Fig. 7   Instantaneous flow field illustrated by Mach number contours and contours of normalized pressure perturbations ($p' = (p - p_\infty)/p_\infty$).

(a) Mean of axial velocity.

(b) RMS of axial velocity.

Fig. 8 **Axial velocity statistics at the nozzle exit: Isolated-1 (——), Isolated-2 (- - - -), Installed-1 (-·-·-), Installed-2 (······), Experiments (○).**

turbulence levels in the region $4 < x_1/D_j < 6$. It is plausible that the underpredicted turbulence levels in this region is connected to the overpredicted mean velocity downstream of the potential core since insufficient turbulent mixing should lead to an elongated potential core.
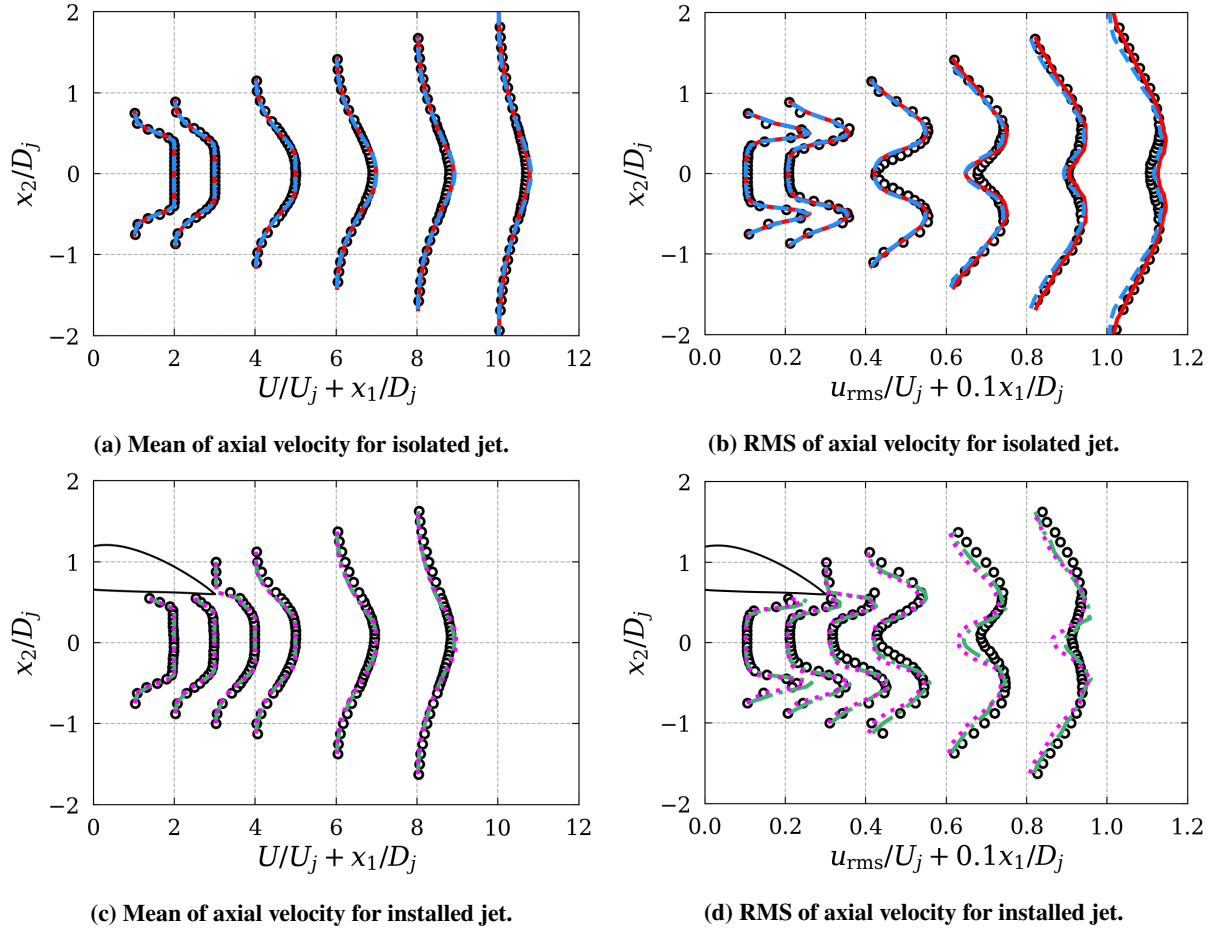
The mean axial velocity for the installed jet is shown in Fig. 9c. As for the isolated jet, the largest discrepancies are found downstream of the potential core, where the simulations of the installed jet overpredict the mean velocity close to the centerline. Apart from this, the agreement between the simulations and the experiments is quite good for all axial locations. Another thing that can be noted from Fig. 9c is that the jet is slightly lifted by the wing due to the Coandă effect. The presence of the wing is also evident when looking at the RMS of the axial velocity, shown in Fig. 9d. In particular, it can be seen that the wing suppresses the turbulence levels in the shear layer, which leads to asymmetric profiles around $1 < x_1/D_j < 3$. Fig. 9d also shows that the turbulence levels are well predicted by the simulations for the installed jet, except close to the centerline for $4 < x_1/D_j < 8$. In this region, the turbulence levels are underpredicted by the simulations.

C. Far-Field Acoustics

As explained in section IV.B, the pressure signal is computed at the microphone locations shown in Fig. 2 using Antares [46–48]. The PSD is then computed from the pressure signal using Welch's method [68], see section IV.B for details. The number of time samples included in each segment in Welch's method was chosen to be $N_{FFT} = 417$ for the Isolated-1 simulation, and $N_{FFT} = 833$ for the remaining simulations. This leads to a bin-size of $\Delta St = D_j/(N_{FFT}\Delta t_{FW-H}U_j) = 0.05$ for all simulations. The Nyquist Strouhal number is further equal to $St_{Nyq} = D_j/(2\Delta t_{FW-H}U_j) = 10.42$ for the Isolated-1 simulation, and $St_{Nyq} = 20.83$ for the remaining simulations. These numbers are approximately twice as large as the highest resolved Strouhal numbers estimated for the corresponding simulation, see Table 2.

The far-field noise obtained for the isolated jet at four representative microphone locations is shown in Fig. 10. The first thing that can be noted from this figure is that the Isolated-2 simulation performs better than the Isolated-1 simulation, especially at lower frequencies. This is likely a result of the higher resolution used in the Isolated-2 simulation, see Fig. 5 for details. However, the agreement between the simulations and the experiments is not perfect. One reason for this is likely the low turbulence levels observed at the nozzle exit. Another thing that can be noted from Fig. 10 is that the simulations agree better with the experiments at low observer angles, i.e., for microphones located far downstream. For high observer angles, on the other hand, the simulations predict a "hump" in the spectra at high frequencies. A similar hump, albeit of smaller amplitude, was recently observed by Gryazev et al. [76] in their LES simulations of the same jet. Finally, we note that the highest resolved Strouhal number is approximately 4 for the Isolated-1 simulation, and 7 for the Isolated-2 simulation. These numbers are approximately 25% lower than the estimates provided in Table 2.

Next, we turn to Fig. 11, which shows the far-field noise on the unshielded side of the installed jet. We start by noting

13

(a) Mean of axial velocity for isolated jet.

(b) RMS of axial velocity for isolated jet.

(c) Mean of axial velocity for installed jet.

(d) RMS of axial velocity for installed jet.

Fig. 9 Axial velocity statistics in the jet plume: Isolated-1 (——), Isolated-2 (- - - -), Installed-1 (-·-·-·), Installed-2 (········), Experiments (○).

14

(a) $\theta = 43°$

(b) $\theta = 71°$

(c) $\theta = 90°$

(d) $\theta = 109°$
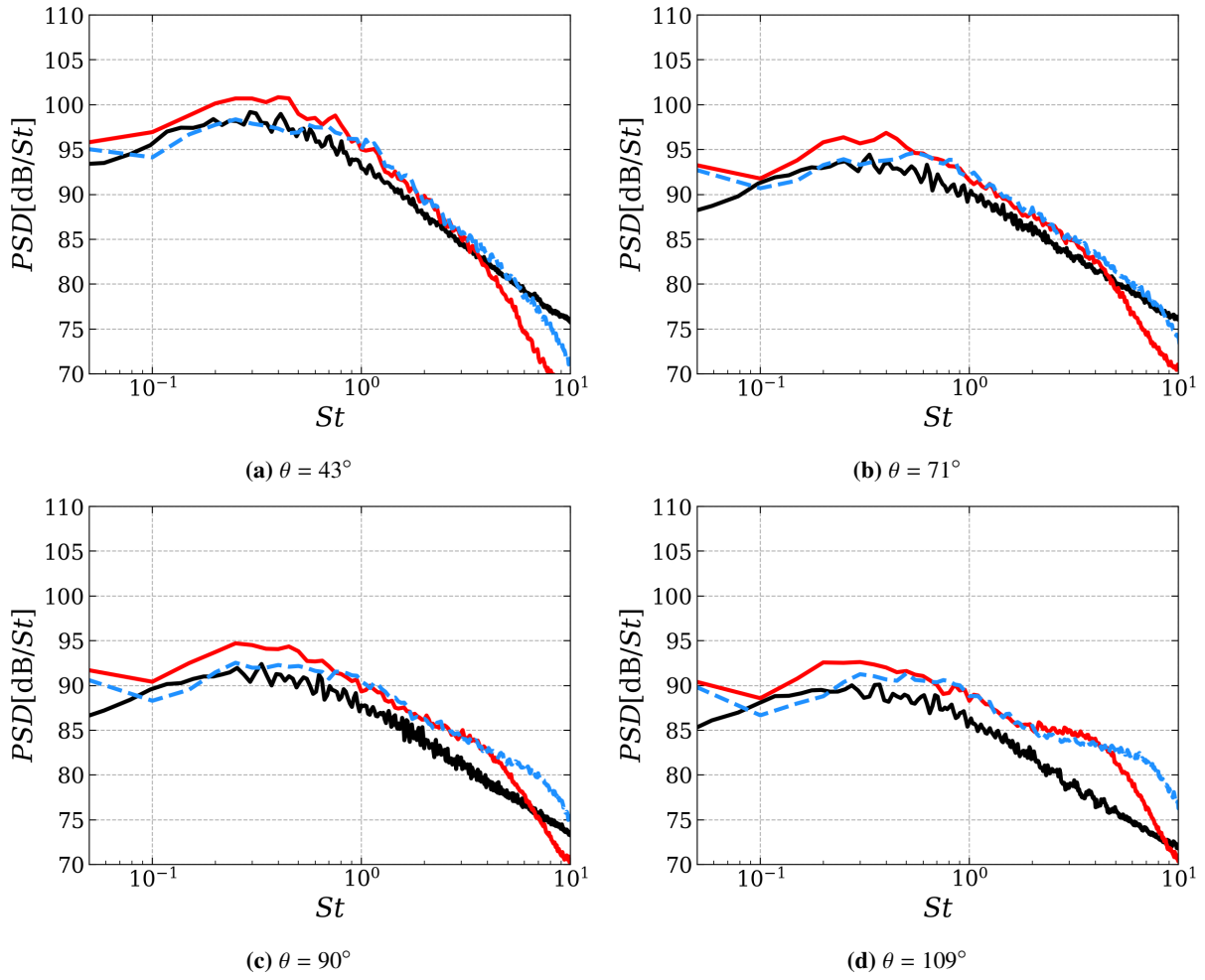
Fig. 10   Power spectral density in the far-field: Isolated-1 (———), Isolated-2 (– – –), Experiments (———).

(a) $\theta = 43°$

(b) $\theta = 71°$

(c) $\theta = 90°$

(d) $\theta = 109°$
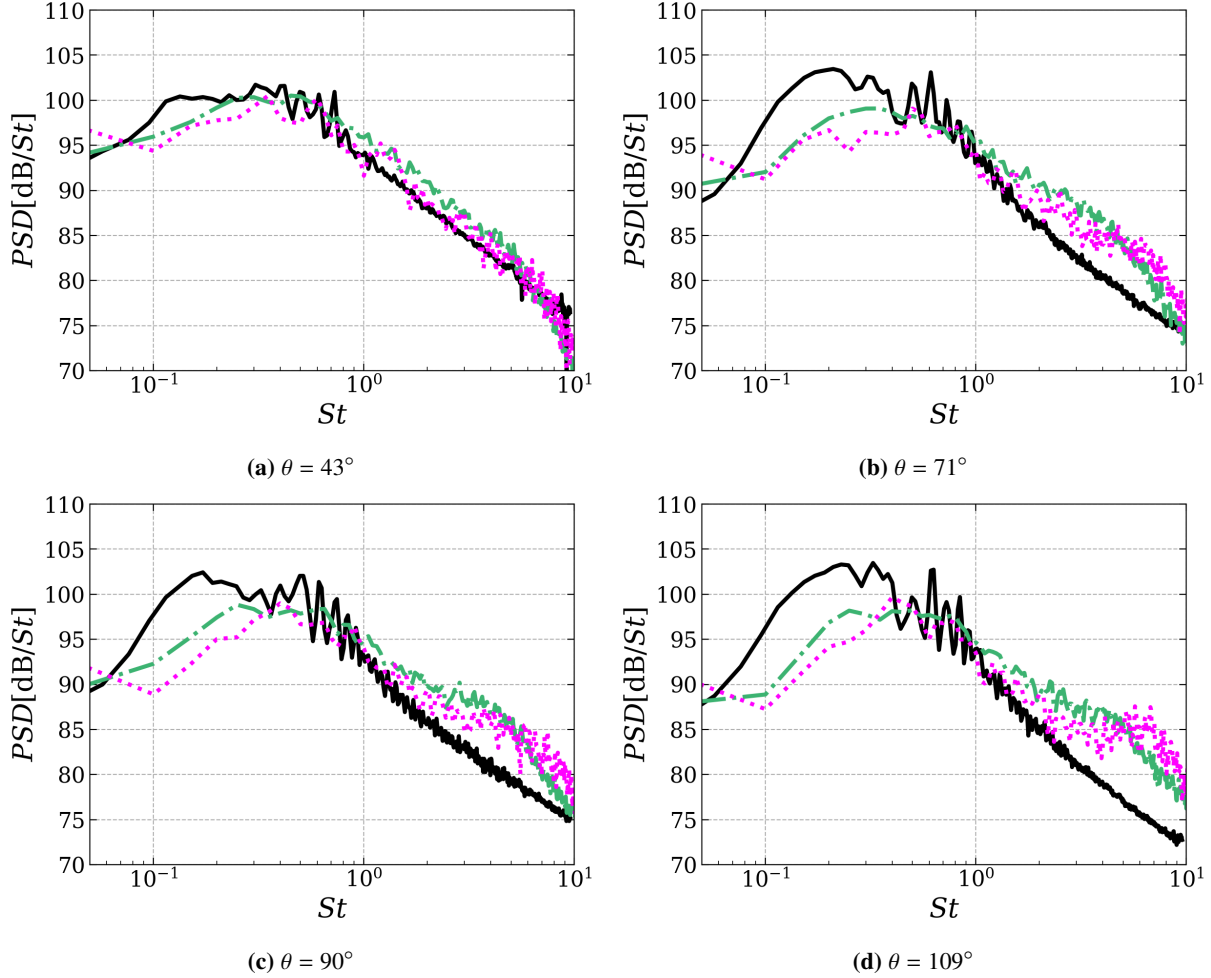
Fig. 11   Power spectral density in the far-field: Installed-1 (–·–·–), Installed-2 (·······), Experiments (——).

that the agreement between the simulations and the experiments is better at low observer angles. This is consistent with the results obtained for the isolated jet. From Fig. 11, we can also see that the noise is underpredicted at low frequencies and overpredicted at high frequencies, especially for higher observer angles. The discrepancies seen at low frequencies could be due to the fact that we use an open integration surface for the Ffowcs Williams - Hawkings method, since this means that one contribution to the integral is lost. With regards to the high frequency noise, we note that it is overpredicted for the isolated jet as well. However, the discrepancies between the simulations and the experiments is larger for the installed jet. To explain this, we note that the amplitude of the highest frequencies will increase on the unshielded side of an installed jet due to reflections from the wing. Therefore, the discrepancies seen for the isolated jet should increase for the installed jet. Due to these humps, it is difficult to estimate the highest resolved Strouhal number for the installed jet. A rough estimate based on the point where the spectra appears to start dropping off considerably is $St_{lim} = 5$ for the Installed-1 simulation and $St_{lim} = 7$ for the Installed-2 simulation.

VII. Conclusions

The noise generated by an isolated and installed jet, both operating at an acoustic Mach number of $M_a = 0.6$ and a Reynolds number of $Re = 5.5 \cdot 10^5$, has been computed using LES. The LES simulations were performed with the spectral/hp element framework Nektar++ [42, 43]. Nektar++ uses the high-order discontinuous Galerkin (DG) method to solve the unfiltered Navier-Stokes equations on unstructured grids [44, 45, 52]. In this work, we used a fully unstructured grid with prism elements close to the walls and tetrahedral elements in the rest of the domain. Two polynomial degrees were used, $P = 2$ and $P = 3$, leading to a third- and fourth-order accurate discretization in space,

respectively. For time integration, a second-order, singly diagonally implicit Runge-Kutta method is used. To compute the far-field noise, Nektar++ was coupled with the Antares library [46–48]. Antares solves the Ffowcs Williams - Hawkings equation [61] for a permeable integration surface [62] in the time domain using a source time dominant algorithm.

The simulation results were compared against experimental data obtained from the Doak Laboratory's Flight Jet Rig, located at the University of Southampton [49]. In terms of flow statistics, the agreement between the simulations and the experimental data is quite good. The most notable discrepancy is found at the nozzle exit, where the simulations run with $P = 2$ underpredict the turbulence levels. This is expected since the resolution of the turbulent boundary layer is not sufficiently high in the simulations. The results improve when $P = 3$ is used, but despite this, there are still notable discrepancies. More sophisticated wall modeling in combination with a higher resolution will be necessary to close this gap. Some discrepancies were also observed close the the centerline in the region $4 < x_1/D_j < 8$. In this region, the simulations overpredict the mean velocity and underpredict the turbulence levels. Similar results have been observed in other LES simulations of the same jet [76]. It is possible that the insufficient resolution of the boundary layer used in this study may contribute to the discrepancies observed further downstream. Another possible cause of the discrepancies is the relatively short section of the nozzle that is included in the simulations. In the experiments, the convergent nozzle is $19D_j$ long, whereas in the simulations, only the last $1.5D_j$ of the nozzle is included. This section may not be long enough for the turbulent boundary layer to develop properly. In addition to this, a purely axial flow is imposed at the inlet to the computational domain. As a result, the radial velocity at the nozzle exit will likely not match the one obtained in the experiments very well. Unfortunately, no data is available to check this.

Previous work has shown that low turbulence levels in the boundary layer may lead to additional far-field noise [21, 27, 67]. The simulations performed in this work confirm these findings. For the isolated jet, the difference between the best simulation and the experiments is approximately 2 dB in the range $0.5 < St < 3$. For Strouhal numbers below 0.5, the agreement is better, whereas for Strouhal numbers above 3, it is slightly worse. The simulations of the installed jet show a similar level of accuracy, except for the lowest frequencies, where notable discrepancies are observed. Despite this, the simulations of the installed jet capture the additional noise generated at the lower frequencies due to installation effects. In addition to this, they capture the additional noise measured at high frequencies on the unshielded side as a result of reflections from the wing.

Acknowledgments

References

[1] European Commission, *Flightpath 2050, Europe's Vision for Aviation*, European Union, 2011. https://doi.org/10.2777/50266.

[2] Lighthill, M. J., "On Sound Generated Aerodynamically. I. General Theory," *Proceedings of the Royal Society of London. Series A, Mathematical and Physical Sciences*, Vol. 211, No. 1107, 1952, pp. 564–587. https://doi.org/10.1098/rspa.1952.0060.

[3] Lighthill, M. J., "On Sound Generated Aerodynamically. II. Turbulence as a Source of Sound," *Proceedings of the Royal Society of London. Series A, Mathematical and Physical Sciences*, Vol. 222, No. 1148, 1954, pp. 1–32. https://doi.org/10.1098/rspa. 1954.0049.

[4] Curle, N., "The Influence of Solid Boundaries upon Aerodynamic Sound," *Proceedings of the Royal Society of London. Series A, Mathematical and Physical Sciences*, Vol. 231, No. 1187, 1955, pp. 505–514. https://doi.org/10.1098/rspa.1955.0191.

[5] Ffowcs Williams, J. E., and Hall, L. H., "Aerodynamic sound generation by turbulent flow in the vicinity of a scattering half plane," *Journal of Fluid Mechanics*, Vol. 40, No. 4, 1970, p. 657–670. https://doi.org/10.1017/S0022112070000368.

[6] Bushell, K., "Measurement and prediction of jet noise in flight," *2nd Aeroacoustics Conference*, Hampton, VA, 1975. https://doi.org/10.2514/6.1975-461.

[7] Head, R., and Fisher, M., "Jet/surface interaction noise - Analysis of farfield low frequency augmentations of jet noise due to the presence of a solid shield," *3rd Aeroacoustics Conference*, Palo Alto, CA, 1976. https://doi.org/10.2514/6.1976-502.

[8] Mead, C., and Strange, P., "Under-wing installation effects on jet noise at sideline," *4th AIAA/CEAS Aeroacoustics Conference*, Toulouse, France, 1998. https://doi.org/10.2514/6.1998-2207.

[9] Lyu, B., Dowling, A. P., and Naqavi, I., "Prediction of installed jet noise," *Journal of Fluid Mechanics*, Vol. 811, 2017, p. 234–268. https://doi.org/10.1017/jfm.2016.747.

[10] Lyrintzis, A. S., and Coderoni, M., "Overview of the Use of Large-Eddy Simulations in Jet Aeroacoustics," *AIAA Journal*, Vol. 58, No. 4, 2020, pp. 1620–1638. https://doi.org/10.2514/1.J058498.

[11] Bodony, D. J., and Lele, S. K., "Current Status of Jet Noise Predictions Using Large-Eddy Simulation," *AIAA Journal*, Vol. 46, No. 2, 2008, pp. 364–380. https://doi.org/10.2514/1.24475.

[12] Brès, G. A., and Lele, S. K., "Modelling of jet noise: a perspective from large-eddy simulations," *Philosophical Transactions of the Royal Society A: Mathematical, Physical and Engineering Sciences*, Vol. 377, No. 2159, 2019, p. 20190081. https://doi.org/10.1098/rsta.2019.0081.

[13] Shur, M. L., Spalart, P. R., and Strelets, M. K., "Noise Prediction for Increasingly Complex Jets. Part I: Methods and Tests," *International Journal of Aeroacoustics*, Vol. 4, No. 3, 2005, pp. 213–245. https://doi.org/10.1260/1475472054771376.

[14] Andersson, N., Eriksson, L.-E., and Davidson, L., "Large-Eddy Simulation of Subsonic Turbulent Jets and Their Radiated Sound," *AIAA Journal*, Vol. 43, No. 9, 2005, pp. 1899–1912. https://doi.org/10.2514/1.13278.

[15] Shur, M. L., Spalart, P. R., and Strelets, M. K., "LES-based evaluation of a microjet noise reduction concept in static and flight conditions," *Journal of Sound and Vibration*, Vol. 330, No. 17, 2011, pp. 4083–4097. https://doi.org/10.1016/j.jsv.2011.02.013.

[16] Brès, G., Nichols, J., Lele, S., and Ham, F., "Towards Best Practices for Jet Noise Predictions with Unstructured Large Eddy Simulations," *42nd AIAA Fluid Dynamics Conference and Exhibit*, New Orleans, LA, 2012. https://doi.org/10.2514/6.2012-2965.

[17] Mendez, S., Shoeybi, M., Sharma, A., Ham, F. E., Lele, S. K., and Moin, P., "Large-Eddy Simulations of Perfectly Expanded Supersonic Jets Using an Unstructured Solver," *AIAA Journal*, Vol. 50, No. 5, 2012, pp. 1103–1118. https://doi.org/10.2514/1.J051211.

[18] Shur, M. L., Spalart, P. R., and Strelets, M. K., "Jet noise computation based on enhanced DES formulations accelerating the RANS-to-LES transition in free shear layers," *International Journal of Aeroacoustics*, Vol. 15, No. 6-7, 2016, pp. 595–613. https://doi.org/10.1177/1475472X16659388.

[19] Lorteau, M., Cléro, F., and Vuillot, F., "Analysis of noise radiation mechanisms in hot subsonic jet from a validated large eddy simulation solution," *Physics of Fluids*, Vol. 27, No. 7, 2015. https://doi.org/10.1063/1.4926792.

[20] Tyacke, J., Naqavi, I., Wang, Z.-N., Tucker, P., and Boehning, P., "Predictive Large Eddy Simulation for Jet Aeroacoustics–Current Approach and Industrial Application," *Journal of Turbomachinery*, Vol. 139, No. 8, 2017. https://doi.org/10.1115/1.4035662.

[21] Brès, G. A., Jordan, P., Jaunet, V., Le Rallic, M., Cavalieri, A. V. G., Towne, A., Lele, S. K., Colonius, T., and Schmidt, O. T., "Importance of the nozzle-exit boundary-layer state in subsonic turbulent jets," *Journal of Fluid Mechanics*, Vol. 851, 2018, p. 83–124. https://doi.org/10.1017/jfm.2018.476.

[22] Tyacke, J. C., Wang, Z.-N., and Tucker, P. G., "LES–RANS of Installed Ultra-High-Bypass-Ratio Coaxial Jet Aeroacoustics with Flight Stream," *AIAA Journal*, Vol. 57, No. 3, 2019, pp. 1215–1236. https://doi.org/10.2514/1.J057057.

[23] Wang, Z.-N., Proenca, A., Lawrence, J., Tucker, P. G., and Self, R., "Large-Eddy-Simulation Prediction of an Installed Jet Flow and Noise with Experimental Validation," *AIAA Journal*, Vol. 58, No. 6, 2020, pp. 2494–2503. https://doi.org/10.2514/1.J058921.

[24] Uzun, A., and Hussaini, M. Y., "Simulation of Noise Generation in the Near-Nozzle Region of a Chevron Nozzle Jet," *AIAA Journal*, Vol. 47, No. 8, 2009, pp. 1793–1810. https://doi.org/10.2514/1.36659.

[25] Uzun, A., Bin, J., and Hussaini, M. Y., "High-Fidelity Numerical Simulation of a Chevron Nozzle Jet Flow," *International Journal of Aeroacoustics*, Vol. 10, No. 5-6, 2011, pp. 531–564. https://doi.org/10.1260/1475-472X.10.5-6.531.

[26] Bogey, C., Marsden, O., and Bailly, C., "Large-eddy simulation of the flow and acoustic fields of a Reynolds number 10^5 subsonic jet with tripped exit boundary layers," *Physics of Fluids*, Vol. 23, No. 3, 2011, pp. 035104–1–035104–20. https://doi.org/10.1063/1.3555634.

[27] Bogey, C., Marsden, O., and Bailly, C., "Influence of initial turbulence level on the flow and sound fields of a subsonic jet at a diameter-based Reynolds number of 10^5," *Journal of Fluid Mechanics*, Vol. 701, 2012, p. 352–385. https://doi.org/10.1017/jfm.2012.162.

[28] Faranosov, G. A., Goloviznin, V. M., Karabasov, S. A., Kondakov, V. G., Kopiev, V. F., and Zaitsev, M. A., "CABARET method on unstructured hexahedral grids for jet noise computation," *Computers and Fluids*, Vol. 88, 2013, pp. 165–179. https://doi.org/10.1016/j.compfluid.2013.08.011.

[29] Bogey, C., and Marsden, O., "Simulations of Initially Highly Disturbed Jets with Experiment-Like Exit Boundary Layers," *AIAA Journal*, Vol. 54, No. 4, 2016, pp. 1299–1312. https://doi.org/10.2514/1.J054426.

[30] Paliath, U., and Premasuthan, S., "Large Eddy Simulation for Jet Installation Effects," *19th AIAA/CEAS Aeroacoustics Conference*, Berlin, Germany, 2013. https://doi.org/10.2514/6.2013-2137.

[31] Mockett, C., Fuchs, M., Kramer, F., Michel, U., Thiele, F., and Steger, M., "Further Development and Initial Validation of Innovative DES-Based Approaches for the Prediction of Jet Noise Installation Effects," *ASME Turbo Expo 2017: Turbomachinery Technical Conference and Exposition*, Charlotte, NC, 2017. https://doi.org/10.1115/GT2017-65253.

[32] Reed, W. H., and Hill, T., "Triangular mesh methods for the neutron transport equation," Technical Report LA-UR-73-479, Los Alamos Scientific Laboratory, 1973.

[33] Cockburn, B., Karniadakis, G. E., and Shu, C.-W., "The Development of Discontinuous Galerkin Methods," *Discontinuous Galerkin Methods*, Springer Berlin Heidelberg, Berlin, Heidelberg, 2000, pp. 3–50. https://doi.org/10.1007/978-3-642-59721-3_1.

[34] Huynh, H. T., "A Flux Reconstruction Approach to High-Order Schemes Including Discontinuous Galerkin Methods," *18th AIAA Computational Fluid Dynamics Conference*, Miami, FL, 2007. https://doi.org/10.2514/6.2007-4079.

[35] Kopriva, D. A., and Kolias, J. H., "A Conservative Staggered-Grid Chebyshev Multidomain Method for Compressible Flows," *Journal of Computational Physics*, Vol. 125, No. 1, 1996, pp. 244–261. https://doi.org/10.1006/jcph.1996.0091.

[36] Kopriva, D. A., "A Conservative Staggered-Grid Chebyshev Multidomain Method for Compressible Flows. II. A Semi-Structured Method," *Journal of Computational Physics*, Vol. 128, No. 2, 1996, pp. 475–488. https://doi.org/10.1006/jcph.1996.0225.

[37] Kopriva, D. A., "A Staggered-Grid Multidomain Spectral Method for the Compressible Navier–Stokes Equations," *Journal of Computational Physics*, Vol. 143, No. 1, 1998, pp. 125–158. https://doi.org/10.1006/jcph.1998.5956.

[38] Liu, Y., Vinokur, M., and Wang, Z., "Spectral difference method for unstructured grids I: Basic formulation," *Journal of Computational Physics*, Vol. 216, No. 2, 2006, pp. 780–801. https://doi.org/10.1016/j.jcp.2006.01.024.

[39] Karniadakis, G., and Sherwin, S., *Spectral/hp Element Methods for Computational Fluid Dynamics*, 2nd ed., Oxford University Press, 2005. https://doi.org/10.1093/acprof:oso/9780198528692.001.0001.

[40] Lorteau, M., de la Llave Plata, M., and Couaillier, V., "Turbulent jet simulation using high-order DG methods for aeroacoustic analysis," *International Journal of Heat and Fluid Flow*, Vol. 70, 2018, pp. 380 – 390. https://doi.org/10.1016/j.ijheatfluidflow.2018.01.012.

[41] Lindblad, D., Sherwin, S., Cantwell, C., Lawrence, J., Proenca, A., and Moragues Ginard, M., "Aeroacoustic Analysis of a Subsonic Jet using the Discontinuous Galerkin Method," *28th AIAA/CEAS Aeroacoustics Conference*, Southampton, UK, 2022. https://doi.org/10.2514/6.2022-2932.

[42] Cantwell, C., Moxey, D., Comerford, A., Bolis, A., Rocco, G., Mengaldo, G., De Grazia, D., Yakovlev, S., Lombard, J.-E., Ekelschot, D., Jordi, B., Xu, H., Mohamied, Y., Eskilsson, C., Nelson, B., Vos, P., Biotto, C., Kirby, R., and Sherwin, S., "Nektar++: An open-source spectral/hp element framework," *Computer Physics Communications*, Vol. 192, 2015, pp. 205 – 219. https://doi.org/10.1016/j.cpc.2015.02.008.

[43] Moxey, D., Cantwell, C. D., Bao, Y., Cassinelli, A., Castiglioni, G., Chun, S., Juda, E., Kazemi, E., Lackhove, K., Marcon, J., Mengaldo, G., Serson, D., Turner, M., Xu, H., Peiró, J., Kirby, R. M., and Sherwin, S. J., "Nektar++: Enhancing the capability and application of high-fidelity spectral/hp element methods," *Computer Physics Communications*, Vol. 249, 2020. https://doi.org/10.1016/j.cpc.2019.107110.

[44] Mengaldo, G., "Discontinuous spectral/hp element methods: development, analysis and applications to compressible flows," Ph.D. thesis, Imperial College London, London, UK, 2015.

[45] Yan, Z.-G., Pan, Y., Castiglioni, G., Hillewaert, K., Peiró, J., Moxey, D., and Sherwin, S. J., "Nektar++: Design and implementation of an implicit, spectral/hp element, compressible flow solver using a Jacobian-free Newton Krylov approach," *Computers & Mathematics with Applications*, Vol. 81, 2021, pp. 351–372. https://doi.org/10.1016/j.camwa.2020.03.009.

[46] antares Development Team, "Antares Documentation Release 1.17.0," , 2020. URL https://cerfacs.fr/antares/.

[47] Di Stefano, D., Rona, A., Hall, E., and Puigt, G., "Implementing the Ffowcs Williams and Hawkings acoustic analogy in Antares," *The 22nd International Congress on Sound and Vibration (ICSV22)*, Florence, Italy, 2015.

[48] Di Stefano, D., Rona, A., Hall, E., Morfey, C. L., and Puigt, G., "Validating the Ffowcs Williams and Hawkings acoustic analogy implementation in Antares," *22nd AIAA/CEAS Aeroacoustics Conference*, Lyon, France, 2016. https://doi.org/10.2514/6.2016-3059.

[49] Proença, A., Lawrence, J., and Self, R., "Experimental Investigation into the Turbulence Flow Field of In-Flight Round Jets," *AIAA Journal*, Vol. 58, No. 8, 2020, pp. 1–11. https://doi.org/10.2514/1.J059035.

[50] Roe, P., "Approximate Riemann solvers, parameter vectors, and difference schemes," *Journal of Computational Physics*, Vol. 43, No. 2, 1981, pp. 357–372. https://doi.org/10.1016/0021-9991(81)90128-5.

[51] Hartmann, R., and Houston, P., "Symmetric Interior Penalty DG Methods for the Compressible Navier-Stokes Equations I: Method Formulation," *International Journal of Numerical Analysis and Modeling*, Vol. 3, No. 1, 2006, pp. 1–20.

[52] Mengaldo, G., Grazia, D. D., Witherden, F., Farrington, A., Vincent, P., Sherwin, S., and Peiro, J., "A Guide to the Implementation of Boundary Conditions in Compact High-Order Methods for Compressible Aerodynamics," *7th AIAA Theoretical Fluid Mechanics Conference*, Atlanta, GA, 2014. https://doi.org/10.2514/6.2014-2923.

[53] Uranga, A., Persson, P.-O., Drela, M., and Peraire, J., "Implicit Large Eddy Simulation of transition to turbulence at low Reynolds numbers using a Discontinuous Galerkin method," *International Journal for Numerical Methods in Engineering*, Vol. 87, No. 1-5, 2011, pp. 232–261. https://doi.org/10.1002/nme.3036.

[54] Beck, A. D., Bolemann, T., Flad, D., Frank, H., Gassner, G. J., Hindenlang, F., and Munz, C.-D., "High-order discontinuous Galerkin spectral element methods for transitional and turbulent flow simulations," *International Journal for Numerical Methods in Fluids*, Vol. 76, No. 8, 2014, pp. 522–548. https://doi.org/10.1002/fld.3943.

[55] Carton de Wiart, C., Hillewaert, K., Bricteux, L., and Winckelmans, G., "Implicit LES of free and wall-bounded turbulent flows based on the discontinuous Galerkin/symmetric interior penalty method," *International Journal for Numerical Methods in Fluids*, Vol. 78, No. 6, 2015, pp. 335–354. https://doi.org/10.1002/fld.4021.

[56] Bergmann, M., Morsbach, C., and Franke, M., *Implicit LES of a Turbulent Channel Flow with High-Order Discontinuous Galerkin and Finite Volume Discretization*, Springer International Publishing, 2019, ERCOFTAC Series, Vol. 25, pp. 61–67. https://doi.org/10.1007/978-3-030-04915-7.

[57] Moura, R., Sherwin, S., and Peiró, J., "Linear dispersion–diffusion analysis and its application to under-resolved turbulence simulations using discontinuous Galerkin spectral/hp methods," *Journal of Computational Physics*, Vol. 298, 2015, pp. 695–710. https://doi.org/10.1016/j.jcp.2015.06.020.

[58] Moura, R., Mengaldo, G., Peiró, J., and Sherwin, S., "On the eddy-resolving capability of high-order discontinuous Galerkin approaches to implicit LES / under-resolved DNS of Euler turbulence," *Journal of Computational Physics*, Vol. 330, 2017, pp. 615–623. https://doi.org/10.1016/j.jcp.2016.10.056.

[59] Mengaldo, G., Moura, R., Giralda, B., Peiró, J., and Sherwin, S., "Spatial eigensolution analysis of discontinuous Galerkin schemes with practical insights for under-resolved computations and implicit LES," *Computers and Fluids*, Vol. 169, 2018, pp. 349–364. https://doi.org/10.1016/j.compfluid.2017.09.016.

[60] Brown, P. N., and Saad, Y., "Convergence Theory of Nonlinear Newton–Krylov Algorithms," *SIAM Journal on Optimization*, Vol. 4, No. 2, 1994, pp. 297–330. https://doi.org/10.1137/0804017.

[61] Ffowcs Williams, J. E., and Hawkings, D. L., "Sound Generation by Turbulence and Surfaces in Arbitrary Motion," *Philosophical Transactions of the Royal Society of London. Series A, Mathematics and Physical Sciences*, Vol. 264, No. 1151, 1969, pp. 321–342. https://doi.org/10.1098/rsta.1969.0031.

[62] di Francescantonio, P., "A New Boundary Integral Formulation for the Prediction of Sound Radiation," *Journal of Sound and Vibration*, Vol. 202, No. 4, 1997, pp. 491–509. https://doi.org/10.1006/jsvi.1996.0843.

[63] Farassat, F., "Derivation of Formulations 1 and 1A of Farassat," Technical Report NASA/TM-2007-214853, NASA, Hampton, VA, March 2007.

[64] Najafi-Yazidi, A., Brès, G. A., and Mongeau, L., "An Acoustic Analogy Formulation for Moving Sources in Uniformly Moving Media," *Proceedings of the Royal Society A, Mathematical, Physical and Engineering Sciences*, Vol. 467, No. 2125, 2011, pp. 144–165. https://doi.org/10.1098/rspa.2010.0172.

[65] Spalart, P. R., and Shur, M. L., "Variants of the Ffowcs Williams - Hawkings Equation and Their Coupling with Simulations of Hot Jets," *International Journal of Aeroacoustics*, Vol. 8, No. 5, 2009, pp. 477–491. https://doi.org/10.1260/147547209788549280.

[66] Mendez, S., Shoeybi, M., Lele, S. K., and Moin, P., "On the Use of the Ffowcs Williams-Hawkings Equation to Predict Far-Field Jet Noise from Large-Eddy Simulations," *International Journal of Aeroacoustics*, Vol. 12, No. 1-2, 2013, pp. 1–20. https://doi.org/10.1260/1475-472X.12.1-2.1.

[67] Zhu, M., Pérez Arroyo, C., Fosso Pouangué, A., Sanjosé, M., and Moreau, S., "Isothermal and heated subsonic jet noise using large eddy simulations on unstructured grids," *Computers and Fluids*, Vol. 171, 2018, pp. 166–192. https://doi.org/10.1016/j.compfluid.2018.06.003.

[68] Welch, P., "The use of fast Fourier transform for the estimation of power spectra: A method based on time averaging over short, modified periodograms," *IEEE Transactions on Audio and Electroacoustics*, Vol. 15, No. 2, 1967, pp. 70–73. https://doi.org/10.1109/TAU.1967.1161901.

[69] Virtanen, P., Gommers, R., Oliphant, T. E., Haberland, M., Reddy, T., Cournapeau, D., Burovski, E., Peterson, P., Weckesser, W., Bright, J., van der Walt, S. J., Brett, M., Wilson, J., Millman, K. J., Mayorov, N., Nelson, A. R. J., Jones, E., Kern, R., Larson, E., Carey, C. J., Polat, İ., Feng, Y., Moore, E. W., VanderPlas, J., Laxalde, D., Perktold, J., Cimrman, R., Henriksen, I., Quintero, E. A., Harris, C. R., Archibald, A. M., Ribeiro, A. H., Pedregosa, F., van Mulbregt, P., and SciPy 1.0 Contributors, "SciPy 1.0: Fundamental Algorithms for Scientific Computing in Python," *Nature Methods*, Vol. 17, 2020, pp. 261–272. https://doi.org/10.1038/s41592-019-0686-2.

[70] Gand, F., and Huet, M., "On the generation of turbulent inflow for hybrid RANS/LES jet flow simulations," *Computers and Fluids*, Vol. 216, 2021. https://doi.org/10.1016/j.compfluid.2020.104816.

[71] Israeli, M., and Orszag, S. A., "Approximation of radiation boundary conditions," *Journal of Computational Physics*, Vol. 41, No. 1, 1981, pp. 115–135. https://doi.org/10.1016/0021-9991(81)90082-6.

[72] Geuzaine, C., and Remacle, J.-F., "Gmsh: A 3-D finite element mesh generator with built-in pre- and post-processing facilities," *International Journal for Numerical Methods in Engineering*, Vol. 79, No. 11, 2009, pp. 1309–1331. https://doi.org/10.1002/nme.2579.

[73] Moxey, D., Green, M., Sherwin, S., and Peiró, J., "An isoparametric approach to high-order curvilinear boundary-layer meshing," *Computer Methods in Applied Mechanics and Engineering*, Vol. 283, 2015, pp. 636–650. https://doi.org/10.1016/j.cma.2014.09.019.

[74] Choi, H., and Moin, P., "Grid-point requirements for large eddy simulation: Chapman's estimates revisited," *Physics of Fluids*, Vol. 24, No. 1, 2012, pp. 011702–1–011702–5. https://doi.org/10.1063/1.3676783.

[75] Jørgensen, F. E., "How to Measure Turbulence with Hot-Wire Anemometers - a Practical Guide," Technical Report, DANTEC Dynamics, Skovlunde, Denmark, 2002.

[76] Gryazev, V., Markesteijn, A., Karabasov, S., Lawrence, J., and Proenca, A., "Flow and Noise Predictions of the Isolated Subsonic Jets from the Doak Laboratory Experiment," *28th AIAA/CEAS Aeroacoustics Conference*, Southampton, UK, 2022. https://doi.org/10.2514/6.2022-2935.